

Realistic Uncertainties for Fundamental Properties of Asteroseismic Red Giants and the Interplay Between Mixing Length, Metallicity and ν_{\max}

YAGUANG LI (李亚光)^{1,2}, TIMOTHY R. BEDDING², DANIEL HUBER^{1,2}, DENNIS STELLO^{3,2}, JENNIFER VAN SADERS¹, YIXIAO ZHOU (周一啸)⁴, COURTNEY L. CRAWFORD², MERIDITH JOYCE^{5,6}, TANDA LI (李坦达)⁷, SIMON J. MURPHY⁸, AND K. R. SREENIVAS²

¹*Institute for Astronomy, University of Hawai'i, 2680 Woodlawn Drive, Honolulu, HI 96822, USA*

²*Sydney Institute for Astronomy (SIfA), School of Physics, University of Sydney, NSW 2006, Australia*

³*School of Physics, University of New South Wales, 2052, Australia*

⁴*Stellar Astrophysics Centre, Department of Physics and Astronomy, Aarhus University, Ny Munkegade 120, DK-8000 Aarhus C, Denmark*

⁵*Konkoly Observatory, HUN-REN Research Centre for Astronomy and Earth Sciences, Konkoly-Thege Miklós út 15-17, H-1121, Budapest, Hungary*

⁶*CSFK, MTA Centre of Excellence, Budapest, Konkoly-Thege Miklós út 15-17, H-1121, Budapest, Hungary*

⁷*Department of Astronomy, Beijing Normal University, Haidian District, Beijing 100875, China*

⁸*Centre for Astrophysics, University of Southern Queensland, Toowoomba, QLD 4350, Australia*

ABSTRACT

Asteroseismic modelling is a powerful way to derive stellar properties. However, the derived quantities are limited by built-in assumptions used in stellar models. This work presents a detailed characterisation of stellar model uncertainties in asteroseismic red giants, focusing on the mixing-length parameter α_{MLT} , the initial helium fraction Y_{init} , the solar abundance scale, and the overshoot parameters. First, we estimate error floors due to model uncertainties to be $\approx 0.4\%$ in mass, $\approx 0.2\%$ in radius, and $\approx 17\%$ in age, primarily due to the uncertain state of α_{MLT} and Y_{init} . The systematic uncertainties in age exceed typical statistical uncertainties, suggesting the importance of their evaluation in asteroseismic applications. Second, we demonstrate that the uncertainties from α_{MLT} can be entirely mitigated by direct radius measurements or partially through ν_{\max} . Utilizing radii from *Kepler* eclipsing binaries, we determined the α_{MLT} values and calibrated the $\alpha_{\text{MLT}}\text{--}[\text{M}/\text{H}]$ relation. The correlation observed between the two variables is positive, consistent with previous studies using 1-D stellar models, but in contrast with outcomes from 3-D simulations. Third, we explore the implications of using asteroseismic modelling to test the ν_{\max} scaling relation. We found that a perceived dependency of ν_{\max} on $[\text{M}/\text{H}]$ from individual frequency modelling can be largely removed by incorporating the calibrated $\alpha_{\text{MLT}}\text{--}[\text{M}/\text{H}]$ relation. Variations in Y_{init} can also affect ν_{\max} predictions. These findings suggest that ν_{\max} conveys information not fully captured by individual frequencies, and that it should be carefully considered as an important observable for asteroseismic modelling.

Keywords: stars: solar-type – stars: oscillations (including pulsations) – stars: low-mass

1. INTRODUCTION

Asteroseismology is the study of stellar structure via stellar oscillations. Ground-based radial velocity instruments and space missions such as CoRoT, Kepler, and TESS have provided extensive data on millions of solar-type stars and red giants. These stars show rich spectra of oscillation modes, enabling a detailed characterisation of stellar interiors (Chaplin & Miglio 2013; Basu & Chaplin 2017).

Driven by advances in observational data, asteroseismology has rapidly become an essential tool for deter-

mining the fundamental properties of field stars, such as age, which are difficult to assess with other methods. One widely used approach, known as forward modelling, involves computing stellar structural models and their standing wave frequencies under varying initial conditions (like mass and chemical composition) and evolving them over time. These models are then matched with asteroseismic parameters derived from observational data.

In red giants, two main types of oscillation modes are excited: pressure (p) modes, which are sound waves probing the envelope cavity, and gravity (g) modes,

which are buoyancy waves probing the core cavity. Asymptotic theory is useful for categorizing these oscillation frequencies (Tassoul 1980; Gough 1986). For p modes with radial order n_p and spherical degree l , the frequencies are approximately evenly spaced:

$$\nu_{n,l} \approx \Delta\nu \left(n_p + \frac{l}{2} + \epsilon_p \right) + \delta\nu_{0,l}. \quad (1)$$

Here, $\Delta\nu$ is the p-mode large separation, which relates to the stellar mean density, $\delta\nu_{0,l}$ is the small separation between modes of different l -degrees, and ϵ_p is a phase offset. For g modes with radial order n_g and spherical degree l , the periods are also roughly evenly spaced:

$$\frac{1}{\nu_{n,l}} \approx \Delta\Pi_l (n_g + \epsilon_{g,l}). \quad (2)$$

Here, $\Delta\Pi_l$ is the g-mode period spacing, and $\epsilon_{g,l}$ is a phase offset. Because these oscillation modes directly probe their respective oscillation cavities, their frequencies or asymptotic parameters are sensitive to the evolving internal structure of stars, providing constraints for stellar ages (Davies & Miglio 2016).

In main-sequence dwarfs, the small separation $\delta\nu_{02}$ is sensitive to the chemical gradient near the core, which changes due to hydrogen burning (Christensen-Dalsgaard 1984). In subgiants, the core contracts while the envelope expands, leading to a phenomenon where g modes in the core couple with p modes in the envelope, with a feature known as an avoided crossing (Deheuvels & Michel 2010; Ong & Basu 2020). At this stage, both the g mode frequencies and the coupling strength change rapidly, making this feature a valuable indicator of stellar age (Li, T. et al. 2020). In red giants, age largely depends on the duration of the main-sequence phase, which is strongly correlated with stellar mass. Since the sizes of the core and envelope are heavily influenced by the stellar mass and radius, both p and g modes are effective tools for estimating the ages of red giants.

Moreover, the observational data also allow for the extraction of amplitudes and damping rates of oscillation modes. However, current models face difficulties in predicting these values due to the complex interaction between convection and pulsation. As a result, the frequency of maximum power, ν_{\max} , is primarily used to constrain models. This is achieved through the application of a scaling relation: $\nu_{\max} \propto g/\sqrt{T_{\text{eff}}} \propto MR^{-2}T_{\text{eff}}^{-1/2}$, where g , M , R , and T_{eff} are the surface gravity, mass, radius, and effective temperature, respectively (Brown et al. 1991; Kjeldsen & Bedding 1995). Despite its extensive application, this scaling relation remains empirical, and its limitations and broader applicability are not fully understood. These issues will be further explored in Section 5.

Using these oscillation frequencies (or asymptotic parameters) and ν_{\max} as constraints, previous studies have consistently reported typical uncertainties of $\approx 4\%$ in mass, $\approx 2\%$ in radius, and $\approx 10\%$ in age for solar-type main-sequence stars and subgiants (e.g. Silva Aguirre et al. 2015, 2017; Li, T. et al. 2020). Similar levels of uncertainty, particularly precision, have also been indicated for red giants (Montalbán et al. 2021; Li, T. et al. 2022). This marks a significant advancement over traditional isochrone fitting methods, which typically yield uncertainties of $\approx 10\%$ in mass and $\approx 50\%$ in age (Tayar et al. 2022).

Given the promising results of asteroseismology, it is crucial to carefully examine the inherent systematic uncertainties in the underlying stellar models. Such uncertainties include the mixing-length parameter α_{MLT} and initial helium abundance Y_{init} , both essential for building stellar models. α_{MLT} is a key parameter in modelling convection, which governs energy transport; Y_{init} shapes the overall chemical composition, affecting the equation of state, opacity, and nuclear reaction rates. However, these parameters can not be determined unambiguously for field stars through observational methods (e.g. Lebreton & Goupil 2014; Appourchaux et al. 2015; Silva Aguirre et al. 2015). One common approach adopted by popular stellar isochrones is to use solar-calibrated values (Demarque et al. 2004; Dotter et al. 2008; Serenelli et al. 2013; Choi et al. 2016; Nguyen et al. 2022), which may not be suitable for the study of field stars given the availability of high-precision observational data, such as those on the lower main sequence (Chen et al. 2014) and the red-giant branch (Tayar et al. 2017; Joyce & Chaboyer 2018b). An alternative method, often employed in the asteroseismic community, involves treating these variables as free parameters in model grid construction, but this practice can obscure other model flaws and still lead to biases in the estimation of stellar properties (Cunha et al. 2021). In practice, the bias in estimating stellar age becomes particularly important in the context of Galactic archaeology, where age scales for millions of red giants have been calibrated based on asteroseismic datasets (Ho et al. 2017; Wu et al. 2018; Wang et al. 2023a; Anders et al. 2023).

In this paper, we aim to scrutinize some of the systematic uncertainties in models, and highlight their significant contribution to the overall uncertainty in determining fundamental stellar properties, especially age, which often surpasses statistical uncertainties. We will assess their impact on estimating stellar properties (Section 3), investigate the interplay between α_{MLT} , radius and metallicity $[M/H]$ (Section 4), and finally, discuss

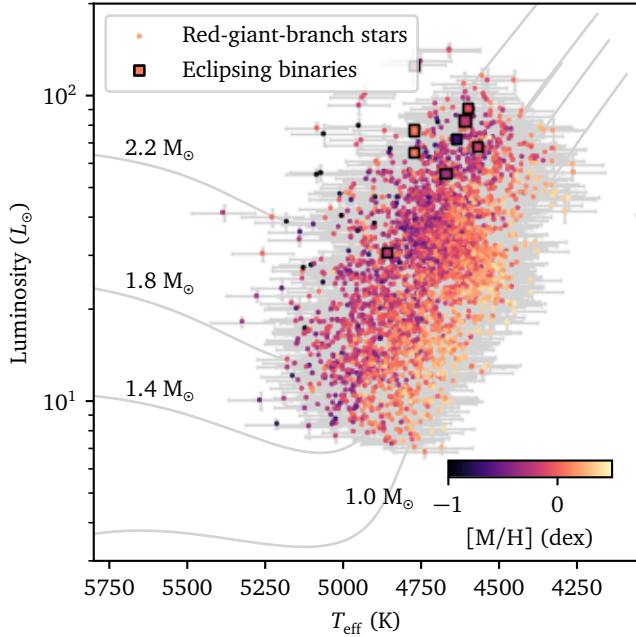


Figure 1. H–R diagram showing the sample used in this work, colour-coded by metallicity. A few solar-metallicity tracks are also shown for visual guidance.

how these model uncertainties affect the validation of the ν_{\max} scaling relation (Section 5).

2. DATA ANALYSIS

2.1. Observations

We first describe the observational data used to constrain stellar models. In this work, we chose the low-luminosity asteroseismic red giants observed by *Kepler* (Yu et al. 2018). We selected our sample (below about $100 L_{\odot}$) by restricting ν_{\max} to be above $17 \mu\text{Hz}$. These low-luminosity red giants are on the red-giant branch (RGB), so contamination from asymptotic-giant-branch (AGB) stars is not a concern. Compared to high-luminosity red giants, these stars exhibit many orders of excited modes, with some of the most comprehensive asteroseismic constraints among all stellar types (Mosser et al. 2011).

For asteroseismic inputs, we collected global oscillation parameters, including ν_{\max} , $\Delta\nu$ and $\Delta\Pi_1$, which are commonly used for optimising stellar models when individual frequencies are unavailable. We chose $\Delta\nu$ values determined by the SYD pipeline (Yu et al. 2018), ν_{\max} values processed by the nuSYD pipeline (Sreenivas et al. 2024). The nuSYD pipeline offers slightly improved precision in ν_{\max} compared to the SYD pipeline (Huber et al. 2009; Yu et al. 2018; Chontos et al. 2021), due to their simple treatment of granulation background and the low-level noise in their adopted PDCSAP (Pre-

search Data Conditioning Simple Aperture Photometry) light curves (Stumpe et al. 2012; Smith et al. 2012). We used $l = 1$ g-mode period spacings ($\Delta\Pi_1$) from Vrad et al. (2016), rather than the individual $l = 1$ oscillation frequencies, to avoid the complexity of treating mixed modes in stellar modelling (Ball et al. 2018).

For the asteroseismic inputs, we also gathered individual frequencies, which are essential for fully utilizing all frequency information from oscillation spectra. We used oscillation frequencies ($l = 0, 2$) extracted by Kallinger (2019), who followed a standard peakbagging approach. However, we did not use the frequencies for $l = 1$ modes, because they are mixed modes, and would require significant computational resources, especially for properly addressing the surface effect (Ong et al. 2021b,a).

For spectroscopic inputs, we used metallicity $[M/H]$ from APOGEE (Pinsonneault et al. 2018; Abdurro’uf et al. 2022), and T_{eff} that we derived from the IRFM method (Casagrande et al. 2021), which uses *Gaia* and 2MASS photometry and extinction values from Green et al. (2019) as inputs. By comparing the IRFM T_{eff} and the APOGEE T_{eff} values, we observed a systematic variation: the IRFM T_{eff} is 50 K higher than the APOGEE values at $[M/H] \sim -0.6$ dex, and conversely, 50 K lower at $[M/H] \sim 0.4$ dex. The root-mean-square difference between the two T_{eff} sources is about 70 K across all $[M/H]$ levels. The differences in T_{eff} scales are likely related to how they were calibrated, rather than being physical. We found that the choice of T_{eff} scale made little difference to our results (see Section 4).

We determined luminosities using K_s -band magnitudes (Cutri et al. 2003), along with Green et al. (2019) extinctions, Choi et al. (2016) bolometric corrections, and *Gaia* DR3 distances (Bailer-Jones et al. 2021).

Furthermore, we included oscillating eclipsing binaries analysed by Gaulme et al. (2016), Brogaard et al. (2018), and Benbakoura et al. (2021), which have masses and radii measured from dynamical modelling. In cases where a star was analysed by multiple studies, we opted for the parameters reported from the most recent study. Figure 1 presents the sample used in this work on the Hertzsprung–Russell diagram.

2.2. Stellar models

We constructed a new set of stellar models with MESA (version r15140; Paxton et al. 2011, 2013, 2015, 2018, 2019) and GRYE (version 6.0.1; Townsend & Teitler 2013). The construction of these models is largely based on the input physics outlined in Li, Y. et al. (2023). The convection was formulated with the mixing-length theory from Henyey et al. (1965) and the surface boundary conditions were constructed with Eddington $T - \tau$ grey

atmosphere model (Eddington 1926). At the end of the paper, we provided a link to the configuration files used for producing the MESA models.

There are two primary differences compared to the Li, Y. et al. (2023) models. Firstly, the new models considered possible variations in the convective overshoot. We used the exponential overshooting scheme according to Herwig (2000), and varied the amount of overshoot for core and shell convective boundaries independently as $f_{\text{ov,core}} \in (0., 0.03)$ and $f_{\text{ov,shell}} \in (0., 0.02)$, respectively. The other free parameters for the grid were initial stellar mass $M \in (0.6, 2.5)$, metallicity $[M/H] \in (-1.0, 0.6)$, the initial helium abundance $Y_{\text{init}} \in (0.20, 0.37)$, and the mixing-length parameter $\alpha_{\text{MLT}} \in (1.0, 2.7)$. No mass loss was included in the models.

Secondly, in addition to calculating the frequencies of the radial modes ($\ell = 0$) we also calculated frequencies of decoupled (pure p) quadrupolar modes ($\ell = 2$) using the method introduced by Ong & Basu (2020). We incorporated the $\ell = 2$ modes in this work because the spacing between $\ell = 0$ and $\ell = 2$ modes, the so-called small separation, relates closely to stellar mass in red giants and could offer extra constraints on stellar properties (Montalbán et al. 2010; Kallinger et al. 2012).

2.3. Model fitting

We followed the model-fitting framework described in Li, Y. et al. (2023). Each model is associated with global stellar parameters $\{M, R, L, \text{Age}, \Delta\Pi_1, T_{\text{eff}}, [M/H], \dots\}$ and oscillation frequencies $\{\nu_i\}$. Following Li, Y. et al. (2023), we corrected the surface effect in $\{\nu_i\}$ with an ensemble approach, which helps eliminate unrealistic surface corrections and reduces scatter in model-derived properties. We achieved this by parameterizing the amount of surface correction at ν_{max} , $\delta\nu_m$, and at 10% above ν_{max} , $\delta\nu'_m$, as functions of stellar surface properties:

$$\delta\nu_m = a \cdot (g/g_\odot)^b \cdot (T_{\text{eff}}/T_{\text{eff},\odot})^c \cdot (d \cdot [M/H] + 1), \quad (3)$$

and

$$\delta\nu'_m = a' \cdot (g/g_\odot)^{b'} \cdot (T_{\text{eff}}/T_{\text{eff},\odot})^{c'} \cdot (d' \cdot [M/H] + 1). \quad (4)$$

These two equations were then used to determine the surface terms (a_{-1} and a_3) in the inverse-cubic correction formula (Ball & Gizon 2014):

$$\delta\nu(\nu; a_{-1}, a_3) = (a_{-1}\nu^{-1} + a_3\nu^3) / \mathcal{I}, \quad (5)$$

where \mathcal{I} is the mode inertia. The parameters appearing in these equations, $\{a, b, c, d, a', b', c', d'\}$, were jointly fitted to the entire sample, yielding best-fitting values of $\{-6.11 \pm 0.28, 0.79 \pm 0.04, -5.04 \pm 0.85, -0.79 \pm$

$0.09, -7.69 \pm 0.72, 0.79 \pm 0.03, -4.59 \pm 0.68, -0.87 \pm 0.08\}$. These values are slightly different from those reported by Li, Y. et al. (2023), due to the differences in underlying models and observational constraints, indicating the importance of such re-calibration for this method.

To determine stellar properties, we applied a range of observational constraints, quantified using chi-squared (χ^2) functions for goodness of fit:

$$\chi_q^2 = \left(\frac{q_{\text{obs}} - q_{\text{mod}}}{\sigma_q} \right)^2, \quad (6)$$

where q represents the observables ν_{max} , $\Delta\Pi_1$, L , T_{eff} , $[M/H]$, M , and R . For individual frequencies, we used reduced χ^2 functions for a group of modes with the same ℓ -degree, which are the standard χ^2 functions averaged by the number of oscillation modes:

$$\chi_l^2 = \frac{1}{N_l} \sum_i^{N_l} \left(\frac{\nu_{\text{obs},l,i} - \nu_{\text{mod},l,i}}{\sigma_{\nu_{\text{obs},l,i}}} \right)^2. \quad (7)$$

In a strict statistical sense, using an average by the number of modes is not appropriate, because each frequency was determined independently. However, these χ^2 functions are very sensitive to inaccurate predictions of mode frequencies, due to the relatively small magnitudes of $\sigma_{\nu_{\text{obs}}}$. Relying on a single set of grid models with a specific selection of input physics (as was done in this work) is unable to fully capture all sources of systematic uncertainties. This limitation could result in extremely large values for the seismic χ^2 functions. Hence, the average method reduces the reliance of the seismic χ^2 on the inaccurate predictions, and quantitatively it is similar to adding an extra error term for systematic uncertainties. We refer the reader to Cunha et al. (2021) for a thorough discussion on this topic.

For illustration, we combine observational constraints into separate groups. The χ_{freq}^2 includes individual frequencies for modes of $l = 0$ and $l = 2$:

$$\chi_{\text{freq}}^2 = \chi_{l=0}^2 + \chi_{l=2}^2. \quad (8)$$

The seismic constraint χ_{seis}^2 incorporates both individual frequencies and global seismic parameters (ν_{max} and $\Delta\Pi_1$):

$$\chi_{\text{seis}}^2 = \chi_{\text{freq}}^2 + \chi_{\nu_{\text{max}}}^2 + \chi_{\Delta\Pi_1}^2. \quad (9)$$

The *Gaia* constraint applies to luminosity:

$$\chi_{\text{Gaia}}^2 = \chi_L^2, \quad (10)$$

and the spectroscopic constraint covers T_{eff} and $[M/H]$:

$$\chi_{\text{spec}}^2 = \chi_{T_{\text{eff}}}^2 + \chi_{[M/H]}^2. \quad (11)$$

For the eclipsing binaries, the dynamical constraint includes mass and radius obtained from the modelling of the binary orbit:

$$\chi_{\text{dyn}}^2 = \chi_M^2 + \chi_R^2. \quad (12)$$

When combining these individual constraints, we implicitly assume that each was derived independently, even though this may not be the case. For example, T_{eff} and $[M/H]$ are often strongly correlated from spectroscopic analysis. To accurately account for such correlations, it is essential to include information on the covariance matrix (e.g. [Gent et al. 2022](#)). However, this information was not available for most of our sample.

Under the Bayesian model-fitting framework, the posterior probability for the model parameters is expressed as

$$p(\theta|\mathcal{D}) = p(\theta) \times \mathcal{L}(\mathcal{D}|\theta), \quad (13)$$

where $p(\theta)$ is the prior on model parameters, which are uniform within the grid boundaries unless noted otherwise. The likelihood function quantifies the agreement between models (specified by θ) and observational data (\mathcal{D}):

$$\mathcal{L}(\mathcal{D}|\theta) = \exp(-\chi^2/2), \quad (14)$$

where χ^2 includes various observational constraints that are detailed in subsequent sections. The estimation of a stellar parameter of interest was determined by integrating Eq. 13 over other model parameters, a process called marginalisation.

3. UNCERTAINTIES FROM MODEL INPUT PHYSICS

3.1. Varying input physics

When studying the effects of varying input physics, [Lebreton et al. \(2014\)](#) identified the most important factors contributing to the uncertainty in the main-sequence lifetime. These include chemical abundances, convective core overshoot, and rotation, with discrepancies surpassing 30% in comparison to a reference model. Chemical abundances and convective core overshoot are especially crucial for low-mass stars above $1.2 M_{\odot}$ (see also [Ying et al. 2023](#); [Joyce et al. 2023](#)). In this section, we look deep into how variations in these two types of input physics influence the inferred stellar properties, in the context of using constraints from asteroseismology.

This investigation was done by adjusting key parameters in our models: the mixing-length parameter α_{MLT} , the initial helium fraction Y_{init} , the solar abundance values $(Z/X)_{\odot}$ used in metallicity calculations, and the core overshoot parameter, $f_{\text{ov,core}}$. Each star was fitted with the full set of observables: $\chi^2 = \chi_{\text{seis}}^2 + \chi_{\text{Gaia}}^2 + \chi_{\text{spec}}^2$.

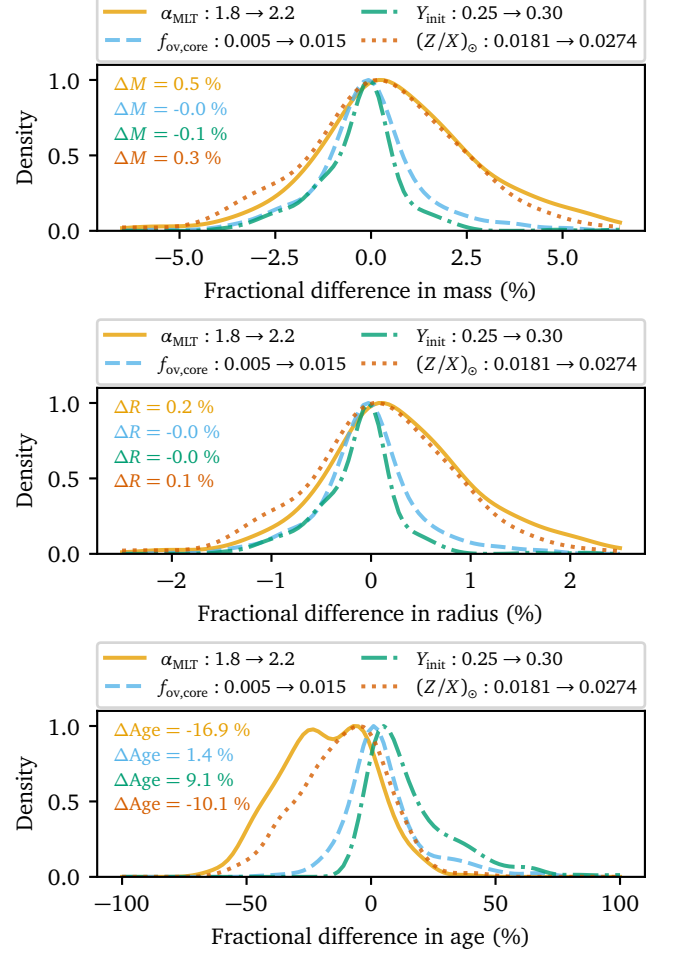


Figure 2. Distributions of the fractional differences in masses, radii, and ages for our red giant sample that result from changing the input physics. Each line corresponds to changing the values of a different model parameter (see legends), and the numbers indicate to the median differences. The distributions have been processed through Gaussian kernel density estimations for clearer visualization. The stellar properties shown in this diagram were derived with $\nu_{\ell=0}$, $\nu_{\ell=2}$, $\Delta\Pi_1$, ν_{max} , T_{eff} , $[M/H]$, and L .

We assessed the fractional differences in stellar properties resulting from these adjustments, with the distributions displayed in Figure 2.

3.1.1. Mixing length

A key focus was on the impact of varying α_{MLT} , which prescribes convective flux transport in convection zones and is especially important in super-adiabatic regions. Although solar-calibrated α_{MLT} values are commonly used in stellar isochrones, several studies advocate for and validate non-solar values across diverse samples (see [Joyce & Tayar 2023](#)). In our analysis, we varied α_{MLT} from 1.8 to 2.2, which covers the range commonly explored in these studies for red giants. The adjustment

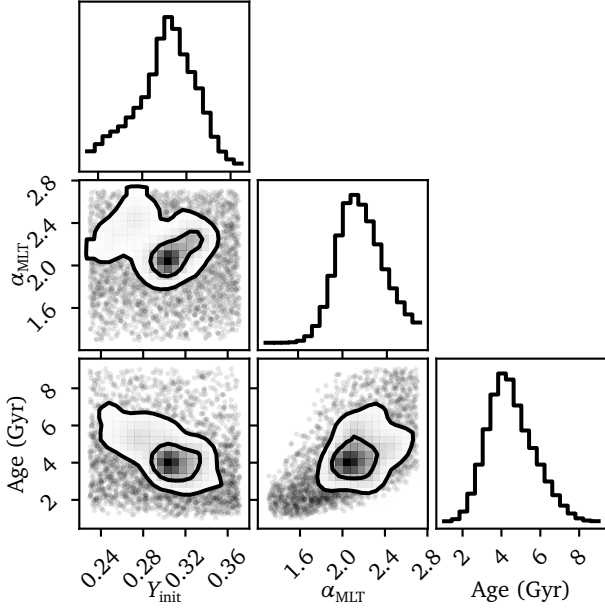


Figure 3. Posterior distributions of stellar models constrained by the observational properties of KIC 10904520. Each point represents a stellar model, colour-coded according to its probability. 1- and 2- σ volumes are displayed as contours.

was implemented by modifying the priors in Eq. 13. For example, setting α_{MLT} to 1.8 involves applying the following normal distribution:

$$\alpha_{\text{MLT}} \sim \mathcal{N}(1.8, \sigma), \quad (15)$$

where $\mathcal{N}(\mu, \sigma)$ denotes a normal distribution with mean μ and standard deviation σ . Here we chose σ as 0.05, and tests showed that using other values (0.025 and 0.1) did not lead to significant differences.

As can be seen from Figure 2, altering α_{MLT} by 0.4 induces the largest variations among the tests we conducted. The median differences are 0.4% in mass, 0.2% in radius, and 16.4% in age. The pronounced α_{MLT} effect on age is indirect, because an increased α_{MLT} tends to favour models with different abundance values that modify ages directly. Specifically, the 0.4 increase in α_{MLT} decreases Y_{init} by ≈ 0.08 , leading to a reduced hydrogen burning rate on the main sequence (Lebreton et al. 2014; McKeever et al. 2019). Moreover, since the metal-to-hydrogen ratio ($[M/H]$ or Z/X) is a fixed constant observational constraint, the change in α_{MLT} raises both X_{init} (by ≈ 0.06) and Z_{init} (by ≈ 0.004). The increase in fuel and the higher opacity during the main sequence both prolong the main-sequence lifespan, substantially increasing the estimated stellar ages (see also Valle et al. 2018). We also note that the sensitivity of α_{MLT} is not dependent on whether T_{eff} is being used.

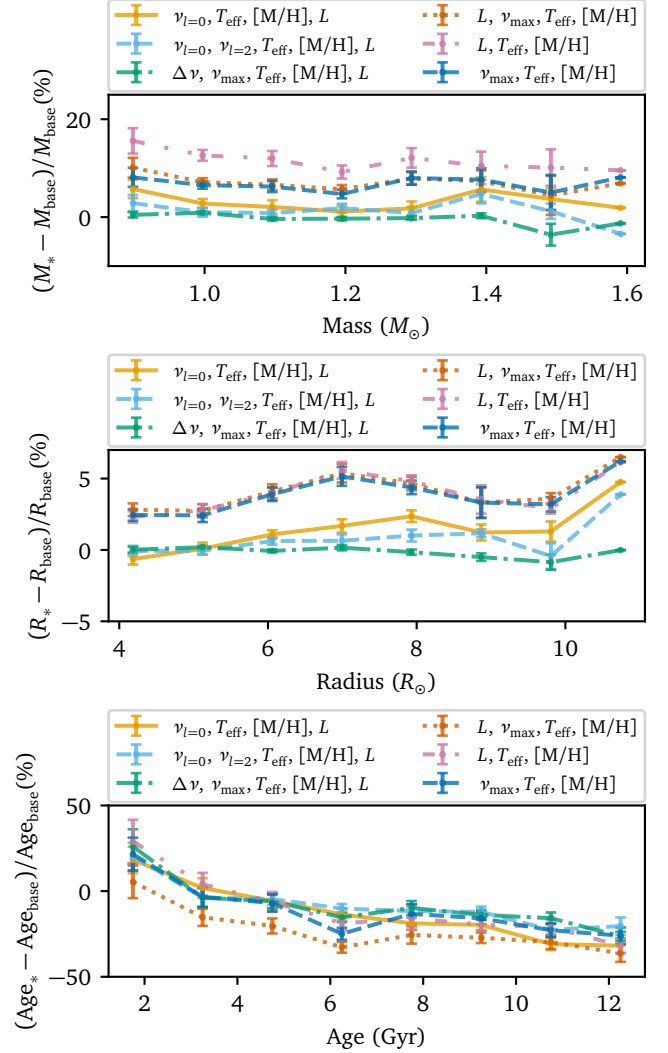


Figure 4. Changes in the derived masses, radii, and ages for our red giant sample that result from changing the input physics. Each point shows the binned medians and the associated errors on the binned medians. In each panel, the x-axis shows the stellar properties derived with $\nu_{\ell=0}$, $\nu_{\ell=2}$, $\Delta\Pi_1$, ν_{max} , T_{eff} , $[M/H]$, and L , denoted as the “base” case. They are compared against the stellar properties derived by other combinations of observational constraints (see legends).

3.1.2. Helium abundance

Due to the lack of photospheric helium lines, direct measurements of helium abundance are challenging, leading to Y_{init} often being treated as a free parameter in stellar modelling. In favorable cases, asteroseismology can measure the helium abundance in the stellar envelope by using the change of the adiabatic index in the HeII ionization zone, which produces oscillatory signatures in p-mode frequencies (Basu & Antia 2004; Broomhall et al. 2014; Verma et al. 2019; Dréau et al. 2020).

Big-bang nucleosynthesis predicts that the primordial helium abundance, Y_p , corresponds to a primordial metal abundance of $Z = 0$. Peimbert & Torres-Peimbert (1974) proposed that the chemical evolution of stars in a galaxy follows

$$Y_{\text{init}} = Y_p + \frac{\Delta Y}{\Delta Z} Z_{\text{init}}, \quad (16)$$

where the coefficient $\Delta Y/\Delta Z$ varies with time and location. Cosmological models estimate Y_p to range from 0.24 to 0.26, setting a lower boundary on Y_{init} (Planck Collaboration et al. 2016). In our Galaxy, $\Delta Y/\Delta Z$ is less well-known, with empirical calibrations suggesting values between 1 and 6 (Jimenez et al. 2003; Casagrande et al. 2007; Verma et al. 2019).

Here, we explore the effects of varying the initial helium abundance Y_{init} . In our analysis, we modified Y_{init} from 0.25 to 0.30, aligning with recent seismic estimations (McKee et al. 2019; Ong et al. 2022). This was implemented by setting priors $Y_{\text{init}} \sim \mathcal{N}(0.25, 0.03)$ and $\mathcal{N}(0.30, 0.03)$. The median differences observed are 0.2% in mass, 0.1% in radius, and 9.0% in age. The age discrepancies, although significant, were less pronounced than those caused by changes in α_{MLT} , as a result of a smaller range of variation in Y_{init} (0.05 in this case as opposed to 0.08). This sensitivity of Y_{init} is also independent of whether T_{eff} is being used.

As an example, in Figure 3 we show the probability distributions of stellar models for KIC 10904520, constrained by $\chi^2_{\text{seis}} + \chi^2_{\text{Gaia}} + \chi^2_{\text{spec}}$. Both Y_{init} and α_{MLT} exhibit correlations with stellar age. This indicates that the values of stellar ages will be heavily affected by priors on α_{MLT} and Y_{init} .

3.1.3. Solar abundance scale

We also examined the effect of different solar abundance scale $(Z/X)_{\odot}$ values. The metallicity ratio $[M/H]$, derived from spectroscopy, implicitly sets a specific solar abundance value $(Z/X)_{\odot}$:

$$[M/H] = \log_{10}(Z/X) - \log_{10}(Z/X)_{\odot}. \quad (17)$$

Various studies have measured $(Z/X)_{\odot}$ ranging between 0.0181 and 0.0274 (Anders & Grevesse 1989; Grevesse & Sauval 1998; Asplund et al. 2009). We tested the effects of these variations by altering the model definition of $[M/H]$, as reflected in χ^2_{spec} . The resulting median differences are 0.3% in mass, 0.1% in radius, and 10.6% in age, showing a similar magnitude of impact as the adjustment in Y_{init} (see also Bellinger et al. 2019).

3.1.4. Overshoot

Lastly, we assessed the effect of changing the core overshoot parameter $f_{\text{ov,core}}$. In stars with masses above

$\sim 1.2 M_{\odot}$, $f_{\text{ov,core}}$ plays a critical role in determining the convective core boundary and the mixing within. Empirical calibrations from asteroseismology and eclipsing binaries suggest that $f_{\text{ov,core}}$ increases with stellar mass. Specifically, $f_{\text{ov,core}}$ starts at 0 for stars of $\approx 1.2 M_{\odot}$ and reaches a stable value of 0.015 for stars above $\approx 2.0 M_{\odot}$ (Tian et al. 2015; Deheuvels et al. 2016; Claret & Torres 2018; Mombarg et al. 2021; Lindsay et al. 2024; Reyes et al. 2024).

We compared two typical values for $f_{\text{ov,core}}$ from these studies, using priors $f_{\text{ov,core}} \sim \mathcal{N}(0.005, 0.005)$ and $\mathcal{N}(0.015, 0.005)$. The changes observed were minimal: negligible in both mass and radius, and 1.0% in age. We also did not find substantial impacts when changing $f_{\text{ov,shell}}$, although its value is known to impact the position of the RGB bump (Christensen-Dalsgaard 2015; Khan et al. 2018).

3.2. Varying the choices of observables

We can gain further insights into the impact of uncertain input physics by comparing the stellar properties derived from different sets of observables. Figure 4 compares the properties derived using various observables against those obtained from the full set: $\chi^2 = \chi^2_{\text{seis}} + \chi^2_{\text{Gaia}} + \chi^2_{\text{spec}}$.

Our first focus concerns models that incorporate asteroseismic constraints only from individual frequencies: $\nu_{\ell=0}$ and $\nu_{\ell=2}$. These models show discrepancies compared to those using the full set, with systematic offsets of up to 5% in mass, 1% in radius, and 15% in age. We also observed a discernible trend in the age discrepancies, correlating with the age itself. These discrepancies are attributed to the inclusion of ν_{max} in the full set, which offers partial constraints on α_{MLT} (discussed in Section 4), leading to a slightly different parameter scale.

We then considered models optimized only by global parameters. We confirmed there are substantial deviations when relying solely on L , T_{eff} , and $[M/H]$, as used in traditional isochrone fitting, with systematic offsets of up to 10% in mass, 2% in radius, and 30% in age, compared to those with the full inputs. When incorporating ν_{max} , either in addition to or as a replacement for L , the discrepancy in radius is similar but the divergence reduces to 5% in mass and by 15% in age. This is because ν_{max} relates to mass with power of 1 (see Eq. 18). The inclusion of ν_{max} , especially for stars beyond 3 kpc where *Gaia* distance measurements are less precise, proves to be very beneficial in improving parameter accuracy (Huber et al. 2017). Furthermore, models incorporating $\Delta\nu$ as an input show excellent consistency with the full seismic inputs. Consequently, we recom-

mend employing a combination of $\Delta\nu$ and ν_{\max} whenever possible, to fully maximize the accuracy of stellar properties (Silva Aguirre et al. 2020).

We compared the masses and ages determined using the full dataset with those determined in earlier studies. Wu et al. (2018) optimized Yonsei–Yale (Y2) stellar models (Demarque et al. 2004) using $\Delta\nu$, ν_{\max} , and spectroscopic parameters from LAMOST spectra. The standard deviations of the fraction differences are 7% for mass and 37% for age. In comparison to Miglio et al. (2021), who optimized MESA models using $\Delta\nu$, ν_{\max} , and spectroscopic parameters from APOGEE spectra, the standard deviations of the fraction differences are 3% for mass and 22% for age. Again, these differences highlight the importance of accounting for systematic uncertainties.

3.3. Summary

Our investigation reveals that the inherent uncertainties in stellar models can lead to significant deviations in the estimated properties of asteroseismic red giants. Specifically, we observed uncertainties up to $\approx 0.4\%$ in mass, $\approx 0.2\%$ in radius and, notably, $\approx 17\%$ in age. The uncertainties mainly stem from the poorly-constrained helium abundance (Y_{init}), which significantly influences other parameters such as the mixing-length parameter (α_{MLT}), initial hydrogen fraction (X_{init}), and initial metallicity (Z_{init}). The age uncertainty is particularly critical, often surpassing the statistical uncertainties commonly reported in individual frequency modelling, which are typically around $\approx 10\%$ (Montalbán et al. 2021; Wang et al. 2023b). Subgiants, on the other hand, offer more reliable age scales (Li, T. et al. 2020; Tayar et al. 2022; Xiang & Rix 2022).

Our results show that, despite integrating constraints from asteroseismic data, a baseline level of systematic uncertainty still persists. This systematic uncertainty sets a realistic lower limit for stellar properties. It is a crucial factor to consider in the application of asteroseismic data for stellar evolution and Galactic archaeology studies.

It is also important to note that, while our study primarily targets RGB stars, the uncertainties for red clump could be even higher due to the accumulation of errors during the earlier evolutionary phases of these stars (Cinquegrana et al. 2023; Noll et al. 2024).

4. CONSTRAINING THE MIXING-LENGTH PARAMETER

4.1. Interplay between α_{MLT} , radius, and ν_{\max}

Our analysis of stellar models, when we omit ν_{\max} as a constraint and rely on $\chi^2 = \chi_{\text{freq}}^2 + \chi_{\text{Gaia}}^2 + \chi_{\text{spec}}^2$, reveals

a notable challenge in precisely determining stellar the radius. This difficulty stems from the lack of constraint on the mixing-length parameter (α_{MLT}). We explain this issue in greater detail below.

In the upper-left panel of Figure 5, we present the posterior distribution of KIC 9540226, marginalised over the α_{MLT} –radius parameter space. It reveals a strong negative and nearly linear correlation between the two parameters under the observational constraints, with a Pearson correlation coefficient of -0.43 . The correlation suggests that accurate determination of either α_{MLT} or radius is challenging without incorporating additional data.

In the upper-middle panel of Figure 5, we introduce an extra constraint, ν_{\max} . Since our 1-D models do not predict amplitudes, the ν_{\max} values were calculated from the scaling relation:

$$\frac{\nu_{\max}}{\nu_{\max,\odot}} \approx \left(\frac{M}{M_{\odot}}\right) \left(\frac{R}{R_{\odot}}\right)^{-2} \left(\frac{T_{\text{eff}}}{T_{\text{eff},\odot}}\right)^{-1/2}, \quad (18)$$

where $\nu_{\max,\odot} = 3090 \mu\text{Hz}$, and $T_{\text{eff},\odot} = 5772 \text{ K}$. This inclusion visibly weakens the correlation (Pearson correlation coefficient reduced to -0.21) because ν_{\max} is proportional to $MR^{-2}T_{\text{eff}}^{-1/2}$, indirectly imposing a constraint on the radius.

In the upper-right panel of Figure 5, we applied additional constraints, χ_{dyn}^2 , related to the mass and radius of KIC 9540266. This effectively neutralizes the correlation between α_{MLT} and radius, allowing for a precise determination of α_{MLT} . Joyce & Chaboyer (2018a) applied a similar approach to the $\alpha \text{ Cen A \& B}$ binary system, demonstrating a relation between α_{MLT} and stellar mass that was preserved across all variations in input physics. We also tested with the radius constraint alone, which yielded similar outcomes. This indicates the importance of direct radius measurements, such as those from interferometry and binary orbit modelling, for calibrating α_{MLT} in stars beyond the Sun.

In the lower panels of Figure 5, we present the posterior distributions now marginalised over the α_{MLT} – ν_{\max} space. We found that precise ν_{\max} determination from models hinges on having α_{MLT} calibrated with direct stellar radius data. It highlights an important point: predicting a reliable ν_{\max} value based solely on individual frequencies is nearly impractical without a predetermined α_{MLT} . This is because the individual frequencies are mostly sensitive to deeper regions within the star, and their sensitivity to super adiabatic near-surface regions is considerably reduced by the empirical surface correction procedure.

4.2. Relation between α_{MLT} and metallicity

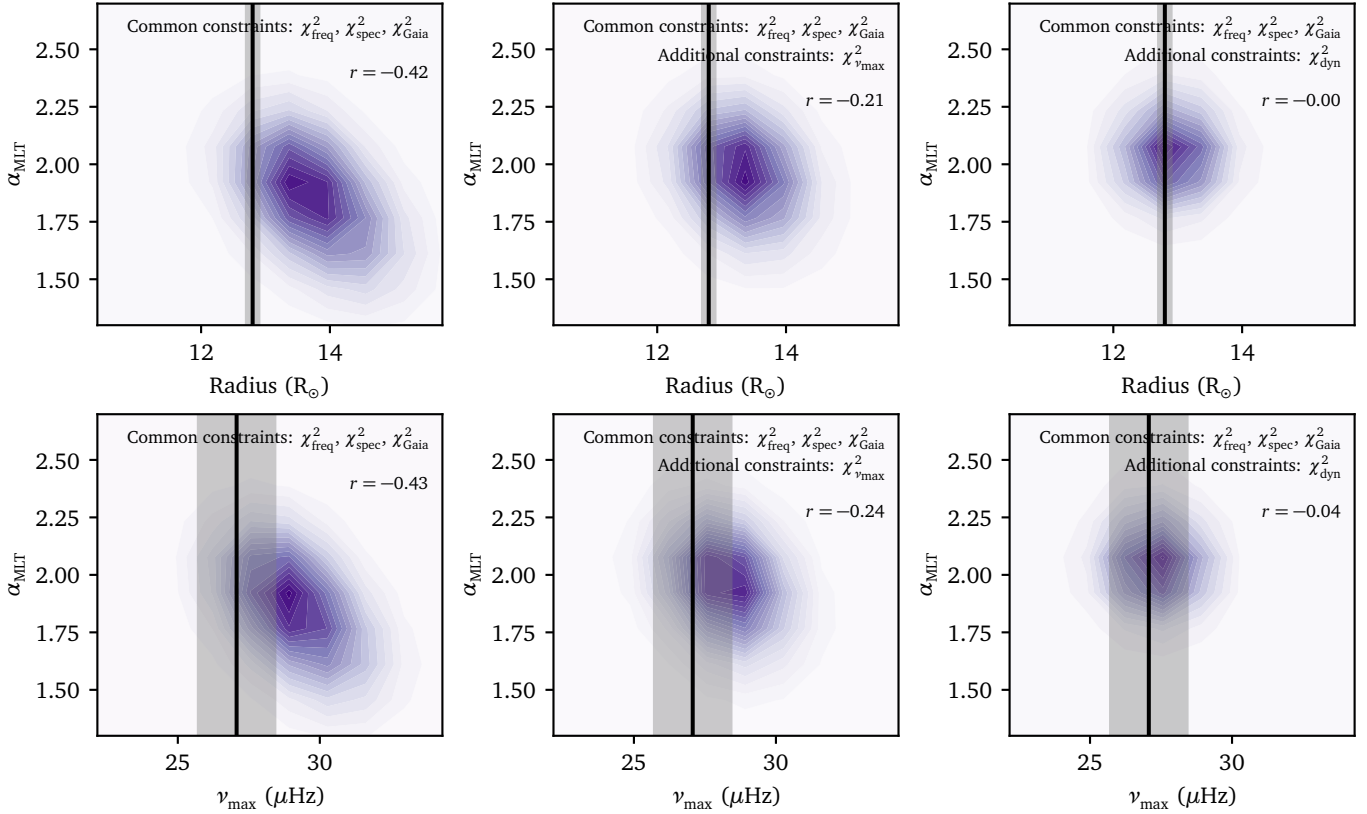


Figure 5. Posterior distributions of stellar models for KIC 9540226 (an eclipsing binary) constrained by $\chi^2 = \chi^2_{\text{freq}} + \chi^2_{\text{spec}} + \chi^2_{\text{Gaia}}$. The top panels show the distributions marginalised in the $(\alpha_{\text{MLT}}, \text{radius})$ space and the bottom panels show those in the $(\alpha_{\text{MLT}}, \nu_{\text{max}})$ space. The panels in the middle column show the results with additional constraint of $\chi^2_{\nu_{\text{max}}}$. The panels in the right column show those with additional constraint of χ^2_{dyn} . The Pearson correlation coefficients calculated from the distributions are displayed in each panel. The vertical lines and the shaded regions show the medians and $1-\sigma$ values for the measured radius (from binary modelling) and the measured ν_{max} (from observed power spectra).

We now turn to examining the relationship between α_{MLT} and $[\text{M}/\text{H}]$. It has been shown in previous studies (such as Metcalfe et al. 2014; Creevey et al. 2017; Tayar et al. 2017; Joyce & Chaboyer 2018b; Viani et al. 2018; Li, T. et al. 2018; Valle et al. 2019) that 1-D stellar models, when constrained by asteroseismic data, often require adjustments in the α_{MLT} values depending the metallicity. This relationship is typically found as a monotonically increasing trend between the two parameters.

We now revisit the $\alpha_{\text{MLT}}-[\text{M}/\text{H}]$ relation, which we intend to constrain with the dynamical mass and radius χ^2_{dyn} . The results are shown in Figure 6. With the χ^2_{dyn} constraints (panel a), we still observe a positive correlation between α_{MLT} and $[\text{M}/\text{H}]$, akin to the pattern found in previous 1-D studies and in models constrained by $\chi^2_{\nu_{\text{max}}}$ (panel b). However, there is a slight difference in the correlation slopes when comparing the two methods. This variation can be attributed to the different effectiveness of $\chi^2_{\nu_{\text{max}}}$ and χ^2_{dyn} in mitigating the correlation between α_{MLT} and radius, as previously dis-

cussed. When neither χ^2_{dyn} nor $\chi^2_{\nu_{\text{max}}}$ are applied (panel c), the correlation between α_{MLT} and $[\text{M}/\text{H}]$ almost vanishes. Therefore, we highlight the importance of having effective calibrations on α_{MLT} for model-based parameter inference. Relying solely on models without such priors could lead to a systematic bias in the derived stellar properties, as we discussed in Section 3.

We also checked the α_{MLT} parameter informed by the Stagger models, a grid of 3-D hydrodynamic simulations of stellar surfaces (Magic et al. 2013). Magic et al. (2015) calibrated α_{MLT} values by matching the entropy values in the nearly adiabatic convection zone of 3-D models with those from corresponding 1-D model atmospheres. We determined the α_{MLT} of our sample by interpolating their calibrated α_{MLT} values at the observed T_{eff} , $[\text{M}/\text{H}]$ and $\log g$ for our sample. The results are shown in Figure 6d, where we do not observe a steep metallicity gradient as seen from 1-D stellar modelling. This discrepancy has been acknowledged by Tayar et al. (2017) and Viani et al. (2018) and the reason is not entirely clear. One possibility is that the helium mass fraction

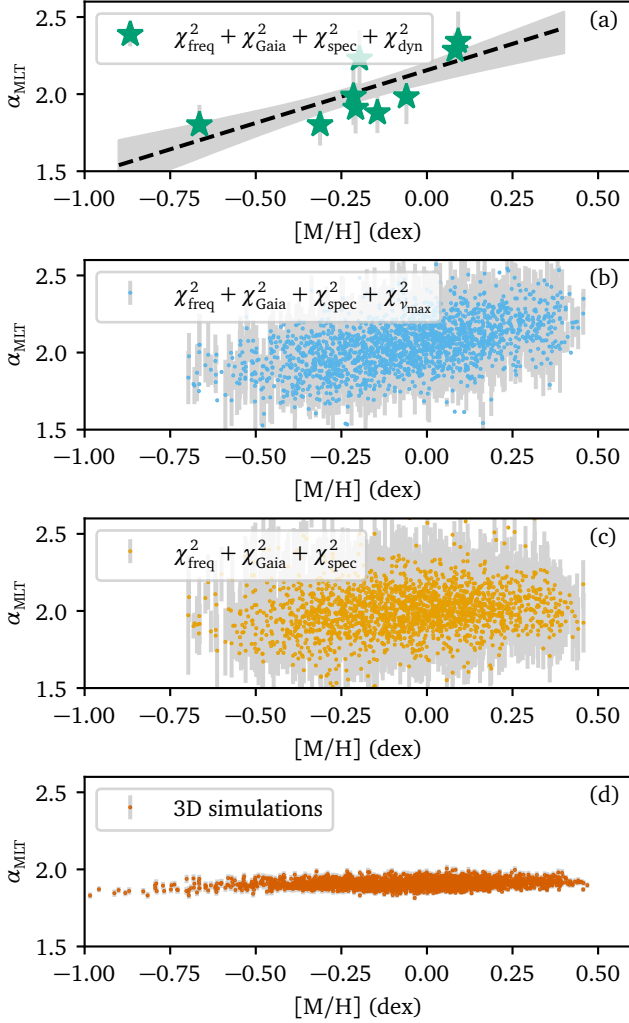


Figure 6. Derived relationships between α_{MLT} and metallicity. Panel (a) shows the 1-D modelling results with the additional χ^2_{dyn} from the binary sample, panel (b) with $\chi^2_{\nu_{\text{max}}}$, and panel (c) with neither of them. Panel (d) shows the interpolated α_{MLT} from 3-D simulations at measured T_{eff} , $[M/H]$ and $\log g$.

Y increases with decreasing metallicity in the Stagger-grid models, which contradicts the Galactic helium enrichment law. Lowering Y in metal-poor 3-D models gives a smaller overall density (Karlsmose 2019), which has a similar effect as lowering the surface gravity hence likely to result in smaller calibrated α_{MLT} (Trampedach et al. 2014; Magic et al. 2015). Had the 3-D simulations constructed following the Helium enrichment law, the expectation is that the positive correlation between $[M/H]$ and calibrated α_{MLT} might be more pronounced.

Using the mass and radius measurements from the eclipsing binary sample, along with the spectroscopic and asteroseismic constraints, we fitted a linear relation

between α_{MLT} and $[M/H]$:

$$\alpha_{\text{MLT}} = (0.66 \pm 0.20) \times [M/H] + (2.14 \pm 0.06). \quad (19)$$

We verified these results by replacing T_{eff} values from those from APOGEE, and found a similar relation:

$$\alpha_{\text{MLT}} = (0.60 \pm 0.14) \times [M/H] + (2.14 \pm 0.06). \quad (20)$$

The slope of α_{MLT} with respect to $[M/H]$ agrees well with the findings of Viani et al. (2018), who modelled stars with $\Delta\nu$, ν_{max} , T_{eff} , and $[M/H]$ and reported a slope of ≈ 0.74 . However, our value appears to be higher than the ≈ 0.16 value found by Tayar et al. (2017), which might be due to their focus on matching T_{eff} instead.

Although we rely on the binary sample to calibrate Eq. 19, we caution that binary stars may be subject to radius inflation. It has been discovered in K and M main-sequence stars that the observed stellar radii are systematically larger than predicted by theoretical models (Torres & Ribas 2002). Magnetic fields (Feiden & Chaboyer 2014) and starspots (Jackson & Jeffries 2014; Somers & Pinsonneault 2015) may be responsible for this discrepancy. Since many red giants in binary systems are magnetically active (Gaulme et al. 2020; Gehan et al. 2024), it is reasonable to conjecture that the radii of these red giant binaries may also be affected by similar issues.

We investigated whether $[M/H]$ is the primary driver for the variability of α_{MLT} in red giants. We calculated the correlation coefficients of α_{MLT} with respect to $[M/H]$, mass, and T_{eff} for the binary sample. They are 0.75, 0.74, and 0.70, respectively, suggesting that a relation with mass or T_{eff} could be equally plausible. However, we have to keep in mind that the binary sample only spans a rather small parameter range. In contrast, for the large asteroseismic sample constrained by ν_{max} , we found those coefficients to be 0.46, 0.10, and 0.02, respectively. Assuming this ν_{max} -constrained scenario is accurate, then $[M/H]$ is indeed the dominant factor influencing variations in α_{MLT} for red giants.

Based on these findings, we adopt Eq. 19 as a preliminary model for further discussions in the subsequent section. We encourage future studies to further refine and validate this relationship as more data from similar systems become available. In particular, more calibrators at lower luminosities and higher metallicities will be especially helpful (see Figure 1).

5. IMPLICATIONS ON TESTING THE ν_{max} SCALING RELATION

5.1. Background

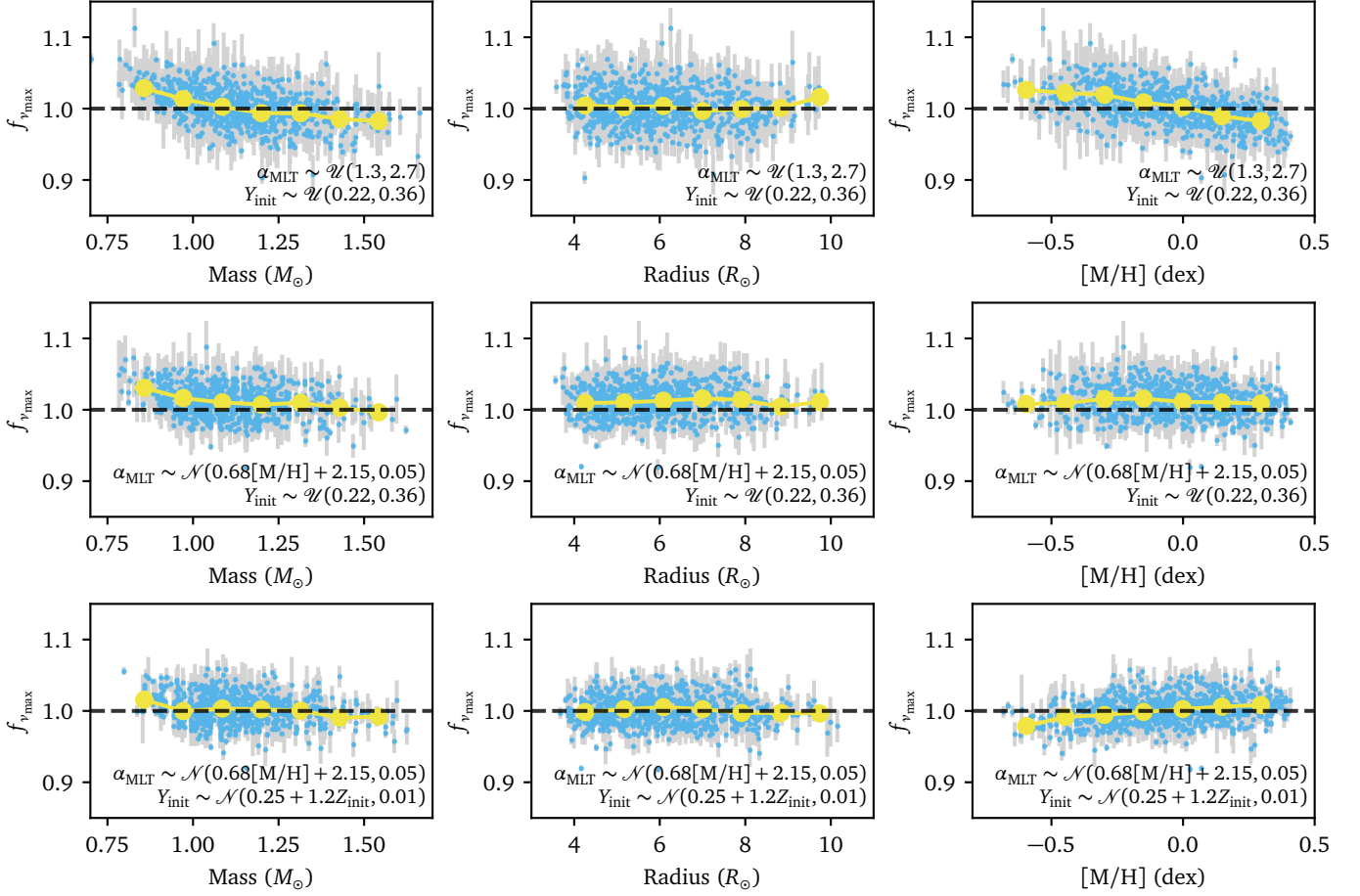


Figure 7. Correction factor of the ν_{\max} scaling relation, $f_{\nu_{\max}}$, as a function of mass, radius, and metallicity (from left to right panels). The top rows show the results obtained without imposing informative priors on α_{MLT} and Y_{init} . The middle rows show those with the calibrated α_{MLT} –[M/H] relation from the eclipsing binary sample. The bottom rows show those with an assumed helium enrichment law.

The ν_{\max} scaling relation is an extremely useful tool for measuring stellar parameters, especially in the current era of extensive ensemble analysis of red giants. Despite its widespread use, the limitations and full scope of this relation are not completely understood (Belkacem et al. 2011; Hekker 2020). In this section, we discuss the test of this scaling relation using 1-D stellar modelling.

The frequency of maximum power, ν_{\max} , is governed by excitation and damping mechanisms, and is therefore inherently a surface property. In this sense, it is different from the individual modes frequencies, which are the resonant frequencies of the entire star. Given that solar-like oscillations are driven and damped by near-surface convection (Goldreich et al. 1994; Samadi et al. 2012; Zhou et al. 2020), it is reasonable to suppose that ν_{\max} , like amplitude, is determined by the surface properties of stars, namely effective temperature, surface gravity and possibly metallicity.

The ν_{\max} scaling relation, originally proposed for main-sequence stars by Brown et al. (1991) and Kjeld-

sen & Bedding (1995), posits that ν_{\max} is a fixed fraction of the acoustic cutoff frequency (ν_{ac}) in the stellar atmosphere, which sets the upper boundary limit for sound waves to remain trapped within the star. Under assumptions of an isothermal atmosphere and ideal gas conditions¹, ν_{ac} can be shown to scale as $\nu_{\text{ac}} \propto g/\sqrt{T_{\text{eff}}}$, where g is the surface gravity and T_{eff} is the effective temperature. To quantify deviation from the scaling relation, we can define a factor $f_{\nu_{\max}}$ as follows (Sharma et al. 2016):

$$\frac{\nu_{\max}}{\nu_{\max,\odot}} = f_{\nu_{\max}} \left(\frac{M}{M_{\odot}} \right) \left(\frac{R}{R_{\odot}} \right)^{-2} \left(\frac{T_{\text{eff}}}{T_{\text{eff},\odot}} \right)^{-1/2}. \quad (21)$$

The ν_{\max} scaling relation has undergone extensive validation against various methodologies, such as astrometry-based luminosities (Silva Aguirre et al. 2012; Huber et al. 2017; Sahlholdt & Silva Aguirre 2018; Hall

¹ These are simplifications that, admittedly, aren't strictly accurate.

et al. 2019; Khan et al. 2019; Zinn et al. 2019), masses and radii from eclipsing binaries (Gaulme et al. 2016; Brogaard et al. 2018; Kallinger et al. 2018; Benbakoura et al. 2021), and the sharpness of population-level features, such as the zero-age main-sequence edge in red giants (Li, Y. et al. 2021).

Two interesting deviations have emerged in the extremes of parameter space. First, there is a noticeable deviation for red giants with radii larger than $\approx 50 R_{\odot}$, of which the reason is not entirely clear (Yu et al. 2020; Zinn et al. 2023). Second, there is a potentially unaccounted-for dependency of ν_{\max} on metallicity, supported by possible correlations seen in model-based stellar parameters (Li, T. et al. 2022; Wang et al. 2023b), and the tendency of ν_{\max} -based stellar mass to be overestimated in metal-poor stars (Epstein et al. 2014; Schonhut-Stasik et al. 2023). An additional metallicity term could resolve these discrepancies.

Indeed, by using a more accurate derivation for sound speed, Viani et al. (2017) proposed that ν_{ac} can also depend on the mean molecular weight and the adiabatic index, thereby introducing a metallicity component (see also Jiménez et al. 2015; Yıldız et al. 2016). However, recent 3-D hydrodynamic atmosphere simulations by Zhou et al. (2023) did not reveal significant variations of ν_{\max} with metallicity, which could be due to a counteracting effect from the Mach number dependency, as suggested by Belkacem et al. (2011).

5.2. Results and discussions

We tested the ν_{\max} scaling relation using the individual frequency modelling approach, similar to prior studies including Metcalfe et al. (2014), Coelho et al. (2015), Li, T. et al. (2022) and Wang et al. (2023b). Our approach involves computing a scaling ν_{\max} according to Eq. 18, using observational properties other than ν_{\max} as constraints: $\chi^2 = \chi_{\text{freq}}^2 + \chi_{\text{Gaia}}^2 + \chi_{\text{spec}}^2$. The derived scaling ν_{\max} is then compared against the actual measured ν_{\max} from power spectra. The ratio of the measured to the derived value is $f_{\nu_{\max}}$ (see Eq. 21). Our method differs from previous studies in two aspects: (1) we incorporate a more comprehensive list of observational constraints including $\ell = 0 - 2$ mode frequencies, to get more precise constraints on the internal structure; (2) we study how model uncertainties affect the derived ν_{\max} .

Figure 7 presents the correction factor $f_{\nu_{\max}}$ as a function of mass, radius, and age. We also employ median values aggregated into bins (displayed as circles), to highlight any systematic trends in $f_{\nu_{\max}}$. Our initial analysis, presented in the top row of the figure, was

conducted without applying informative priors on α_{MLT} and Y_{init} . These results indicate a negative correlation of $f_{\nu_{\max}}$ with both mass and metallicity. Such findings could lead to the conclusions that adjustments to the ν_{\max} scaling relation are necessary. The correlation with $[M/H]$ is especially tempting, considering the previously discussed influence of $[M/H]$.

However, it is essential to approach these trends cautiously. Our previous discussions suggest that α_{MLT} is not adequately constrained even with asteroseismic frequencies. Thus, employing non-informative priors on α_{MLT} can result in systematically biased stellar parameters. To address this, we used a normal prior on α_{MLT} around the value given by Eq. 19:

$$\alpha_{\text{MLT}} \sim \mathcal{N}(0.68[M/H] + 2.15, 0.05). \quad (22)$$

The resulting $f_{\nu_{\max}}$ is shown in the middle row of Figure 7. The trend with $[M/H]$ vanishes when we incorporate the calibrated $\alpha_{\text{MLT}}-[M/H]$ relation. The trend with mass also greatly reduces.

Interestingly in this case, we noticed that the $f_{\nu_{\max}}$ factor consistently exceeds 1, hinting at a possible need to adjust the reference values in Eq. 18 for red giants from the current solar-based values. Yet, this adjustment may not be necessary if we apply specific priors to Y_{init} . We implemented a normal prior for Y_{init} based on the Galactic enrichment law:

$$Y_{\text{init}} \sim \mathcal{N}(Y_p + \frac{\Delta Y}{\Delta Z} Z_{\text{init}}, 0.01), \quad (23)$$

with $Y_p = 0.25$ and $\Delta Y/\Delta Z = 1.2$, although the value for $\Delta Y/\Delta Z$ is subject to debate. The outcomes of this implementation are shown in the bottom row of Figure 7. We observed that the $f_{\nu_{\max}}$ correction factor closely aligns with 1, suggesting no significant deviation from the standard scaling relation. We also note that in this case $f_{\nu_{\max}}$ presents a positive correlation with $[M/H]$, which can be easily destructed again with a slightly different prescription for α_{MLT} .

From these findings, we conclude that testing the ν_{\max} scaling relation through individual frequency modelling does not always yield conclusive results and requires a thorough consideration of model uncertainties, especially α_{MLT} and Y_{init} . Additionally, we may also expect that other model assumptions, such as the atmosphere boundary condition (Choi et al. 2018; Salaris et al. 2018) and the treatment of surface correction (Li, Y. et al. 2023), modify the surface layers and influence the derived scaling ν_{\max} .

Our findings also indicate that ν_{\max} imparts unique information distinct from individual frequencies. Therefore, ν_{\max} should be regarded as a valuable constraint in asteroseismic modelling.

5.3. Recommendations for using the ν_{\max} scaling relation

We recommend practices for using ν_{\max} to derive stellar properties. Most ν_{\max} extraction pipelines only consider the statistical uncertainties for measuring ν_{\max} , which sometimes could be smaller than the total error budget. Below we list some of the external sources of uncertainties.

First, the values of ν_{\max} is influenced by the method in which stellar oscillation was detected. ν_{\max} is affected by the wavelength range of the photometric filters used, as well as whether observations are conducted through radial velocity or photometry. Such factors can result in $\approx 5\%$ discrepancies in ν_{\max} in the Sun (Howe et al. 2020). Moreover, differences in the treatment of power spectra among data reduction pipelines can lead to differences in ν_{\max} for about 2% (Pinsonneault et al. 2018). Therefore, when the studied samples are not characterised with the same instrument or the same data reduction pipeline, it is crucial to account for these additional sources of discrepancy.

Second, ν_{\max} changes over time due to astrophysical origins. For example, ν_{\max} is subject to variations with magnetic cycles. The Sun varies ν_{\max} of $\approx 0.8\%$ in a solar cycle (Howe et al. 2020). In addition, the stochastic nature of oscillations can cause ν_{\max} to fluctuate over fixed lengths of observing windows. In the case of *Kepler* red giants, typical scatter in ν_{\max} ranges from 2% to 5% in three-month observing windows (Sreenivas et al. 2024). This issue is even more troublesome for some TESS stars with only one sector of data (e.g. Jiang et al. 2023). Hence, these types of uncertainties need to be quantified, presumably via simulations, especially if ν_{\max} is measured with short time series.

After accounting for the various sources of uncertainty associated with ν_{\max} , we advocate for its integration into stellar modelling. As detailed in Section 5.2, ν_{\max} provides constraints distinct from those obtained from individual frequencies. Furthermore, as illustrated in Section 4.2, incorporating ν_{\max} assists in reducing the uncertainty in the mixing-length parameter, α_{MLT} . This reduction is especially helpful for reducing uncertainties in stellar age, which arises from mutual effects of α_{MLT} and Y_{init} (Section 3).

6. CONCLUSIONS

In our study, we present a detailed characterisation of red giant model uncertainties, focusing on the impact of the mixing-length parameter α_{MLT} , the initial helium fraction Y_{init} , the solar abundance scale $(Z/X)_{\odot}$, and the core overshoot parameter $f_{\text{ov,core}}$. Our objective is to understand how these factors influence the determi-

nation of stellar mass, radius, and age in asteroseismic modelling. The key conclusions are summarised as follows:

1. We identified that uncertainties in α_{MLT} and Y_{init} significantly affect the accuracy of stellar properties, despite incorporating constraints from spectroscopy (T_{eff} , $[M/H]$), *Gaia* astrometry (L), and asteroseismology ($\nu_{\ell=0}$, $\nu_{\ell=2}$, ν_{\max} , $\Delta\Pi_1$). These uncertainties set an error floor on mass of $\approx 0.4\%$, radius of $\approx 0.2\%$, and age of $\approx 17\%$ (Figure 2). The error floors due to model uncertainties in age exceed typical statistical uncertainties $\approx 10\%$, showing the importance of their evaluation in asteroseismic applications.
2. We examined the effect of different combinations of observational constraints (Figure 4). Incorporating asteroseismic constraints only from individual frequencies shows discrepancies compared to the case of using the full set of inputs that include ν_{\max} , suggesting ν_{\max} sets a slightly different parameter scale, due to its constraining ability on α_{MLT} . In addition, incorporating asteroseismic constraints from $\Delta\nu$ and ν_{\max} shows excellent consistency with the full set of inputs. Therefore, for ensemble analysis of red giants, a combination of $\Delta\nu$ and ν_{\max} should be included wherever possible.
3. We showed that an uncertain state of α_{MLT} translates to uncertain predictions on stellar radius and ν_{\max} (Figure 5). Hence, direct and accurate measurements of stellar radius will enable the calibration of α_{MLT} , such as those from eclipsing binaries or interferometry. More calibrators are needed in order to fully address this uncertainty.
4. Using a small *Kepler* eclipsing binary sample, for which dynamical radii have been determined, we calibrated the relation between α_{MLT} and $[M/H]$ (Eq. 19 and Figure 6). We observed a positive correlation, consistent with previous 1-D stellar asteroseismic modelling that does not use the extra constraints from binaries. The result remains in tension with 3-D simulations, possibly due to differing treatments of helium abundances.
5. We showed that predicting a reliable ν_{\max} value based solely on individual frequencies is nearly impractical (Figure 5). The model-derived scaling ν_{\max} , shows strong dependence on the uncertainties in both α_{MLT} and Y_{init} , which prohibits accuracy tests on the ν_{\max} scaling relation from mode frequency modelling (Figure 7).

6. We concluded that ν_{\max} provides distinct information and should be considered as an important observable in asteroseismic modelling, and provided our guidelines for its usage in Section 5.3.

ACKNOWLEDGEMENTS

Y.L. expresses gratitude to Bill Chaplin and Margarida Cunha for their thorough and constructive comments during his PhD exam process. Y.L. acknowledges the support by the Beatrice Watson Parrent Fellowship and the National Aeronautics and Space Administration (80NSSC19K0597). We acknowledge support from the Australian Research Council for T.R.B (DP210103119 and FL220100117), D.S. (DP190100666) and S.J.M (FT210100485). D.H. acknowledges support from the Alfred P. Sloan Foundation and the Australian Research Council (FT200100871). M.J. is supported by the Horizon 2020 research and innovation programme’s funding of MATISSE: *Measuring Ages Through Isochrones, Seismology, and Stellar Evolution*.

Funding for the Kepler mission is provided by the NASA Science Mission Directorate. This paper includes data collected by the Kepler mission and obtained from the MAST data archive at the Space Telescope Science Institute (STScI). STScI is operated by the Association of Universities for Research in Astronomy, Inc., under NASA contract NAS 5–26555.

This work presents results from the European Space Agency (ESA) space mission Gaia. Gaia data are be-

ing processed by the Gaia Data Processing and Analysis Consortium (DPAC). Funding for the DPAC is provided by national institutions, in particular the institutions participating in the Gaia MultiLateral Agreement (MLA).

The APOGEE data is from the Sloan Digital Sky Survey IV, whose funding has been provided by the Alfred P. Sloan Foundation, the U.S. Department of Energy Office of Science, and the Participating Institutions.

We acknowledge the Sydney Informatics, the University of Sydney’s high performance computing (HPC) cluster Artemis, and the University of Hawaii’s Information Technology Services – Cyberinfrastructure (funded in part by the National Science Foundation CC* awards #2201428 and #2232862), for providing the HPC resources that have contributed to the research results reported within this paper.

Software: Numpy (van der Walt et al. 2011), Scipy (Virtanen et al. 2020), Matplotlib (Hunter 2007), Astropy (Astropy Collaboration et al. 2013, 2018, 2022), Pandas (Wes McKinney 2010), MESA (Paxton et al. 2011, 2013, 2015, 2018, 2019; Jermyn et al. 2023), MESASDK (Townsend 2020), GYRE (Townsend & Teitler 2013), Lightkurve (Lightkurve Collaboration et al. 2018), ISOCCLASSIFY (Huber et al. 2017; Berger et al. 2020), colte (Casagrande et al. 2021), GPT-4 (OpenAI 2023). The analysis scripts, MESA inlists and MESA models used in this work are available at GitHub (link)² and Zenodo (cite DOI).

REFERENCES

- Abdurro’uf, Accetta, K., Aerts, C., et al. 2022, ApJS, 259, 35
- Anders, E., & Grevesse, N. 1989, GeoCoA, 53, 197
- Anders, F., Gispert, P., Ratcliffe, B., et al. 2023, A&A, 678, A158
- Appourchaux, T., Antia, H. M., Ball, W., et al. 2015, A&A, 582, A25
- Asplund, M., Grevesse, N., Sauval, A. J., & Scott, P. 2009, ARA&A, 47, 481
- Astropy Collaboration, Robitaille, T. P., Tollerud, E. J., et al. 2013, A&A, 558, A33
- Astropy Collaboration, Price-Whelan, A. M., Sipőcz, B. M., et al. 2018, AJ, 156, 123
- Astropy Collaboration, Price-Whelan, A. M., Lim, P. L., et al. 2022, ApJ, 935, 167
- Bailer-Jones, C. A. L., Rybizki, J., Fouesneau, M., Demleitner, M., & Andrae, R. 2021, AJ, 161, 147
- Ball, W. H., & Gizon, L. 2014, A&A, 568, A123
- Ball, W. H., Themeßl, N., & Hekker, S. 2018, MNRAS, 478, 4697
- Basu, S., & Antia, H. M. 2004, ApJL, 606, L85
- Basu, S., & Chaplin, W. J. 2017, Asteroseismic Data Analysis: Foundations and Techniques
- Belkacem, K., Goupil, M. J., Dupret, M. A., et al. 2011, A&A, 530, A142
- Bellinger, E. P., Hekker, S., Angelou, G. C., Stokholm, A., & Basu, S. 2019, A&A, 622, A130
- Benbakoura, M., Gaulme, P., McKeever, J., et al. 2021, arXiv e-prints, arXiv:2101.05351
- Berger, T. A., Huber, D., van Saders, J. L., et al. 2020, AJ, 159, 280
- Brogaard, K., Hansen, C. J., Miglio, A., et al. 2018, MNRAS, 476, 3729
- Broomhall, A. M., Miglio, A., Montalbán, J., et al. 2014, MNRAS, 440, 1828

² insert Github link upon publication.

- Brown, T. M., Gilliland, R. L., Noyes, R. W., & Ramsey, L. W. 1991, *ApJ*, 368, 599
- Casagrande, L., Flynn, C., Portinari, L., Girardi, L., & Jimenez, R. 2007, *MNRAS*, 382, 1516
- Casagrande, L., Lin, J., Rains, A. D., et al. 2021, *MNRAS*, 507, 2684
- Chaplin, W. J., & Miglio, A. 2013, *ARA&A*, 51, 353
- Chen, Y., Girardi, L., Bressan, A., et al. 2014, *MNRAS*, 444, 2525
- Choi, J., Dotter, A., Conroy, C., et al. 2016, *ApJ*, 823, 102
- Choi, J., Dotter, A., Conroy, C., & Ting, Y.-S. 2018, *ApJ*, 860, 131
- Chontos, A., Huber, D., Sayeed, M., & Yamsiri, P. 2021, arXiv e-prints, arXiv:2108.00582
- Christensen-Dalsgaard, J. 1984, in *Space Research in Stellar Activity and Variability*, ed. A. Mangeney & F. Praderie, 11
- Christensen-Dalsgaard, J. 2015, *MNRAS*, 453, 666
- Cinquegrana, G. C., Joyce, M., & Karakas, A. I. 2023, *MNRAS*, 525, 3216
- Claret, A., & Torres, G. 2018, *ApJ*, 859, 100
- Coelho, H. R., Chaplin, W. J., Basu, S., et al. 2015, *MNRAS*, 451, 3011
- Creevey, O. L., Metcalfe, T. S., Schultheis, M., et al. 2017, *A&A*, 601, A67
- Cunha, M. S., Roxburgh, I. W., Aguirre Børsen-Koch, V., et al. 2021, *MNRAS*, 508, 5864
- Cutri, R. M., Skrutskie, M. F., van Dyk, S., et al. 2003, *2MASS All Sky Catalog of point sources*.
- Davies, G. R., & Miglio, A. 2016, *Astronomische Nachrichten*, 337, 774
- Deheuvels, S., Brandão, I., Silva Aguirre, V., et al. 2016, *A&A*, 589, A93
- Deheuvels, S., & Michel, E. 2010, *Ap&SS*, 328, 259
- Demarque, P., Woo, J.-H., Kim, Y.-C., & Yi, S. K. 2004, *ApJS*, 155, 667
- Dotter, A., Chaboyer, B., Jevremović, D., et al. 2008, *ApJS*, 178, 89
- Dréau, G., Cunha, M. S., Vrad, M., & Avelino, P. P. 2020, *MNRAS*, 497, 1008
- Eddington, A. S. 1926, *The Internal Constitution of the Stars* (The University Press)
- Epstein, C. R., Elsworth, Y. P., Johnson, J. A., et al. 2014, *ApJL*, 785, L28
- Feiden, G. A., & Chaboyer, B. 2014, *ApJ*, 789, 53
- Gaulme, P., McKeever, J., Jackiewicz, J., et al. 2016, *ApJ*, 832, 121
- Gaulme, P., Jackiewicz, J., Spada, F., et al. 2020, *A&A*, 639, A63
- Gehan, C., Godoy-Rivera, D., & Gaulme, P. 2024, *A&A*, 686, A93
- Gent, M. R., Bergemann, M., Serenelli, A., et al. 2022, *A&A*, 658, A147
- Goldreich, P., Murray, N., & Kumar, P. 1994, *ApJ*, 424, 466
- Gough, D. O. 1986, in *Hydrodynamic and Magnetodynamic Problems in the Sun and Stars*, ed. Y. Osaki, 117
- Green, G. M., Schlafly, E., Zucker, C., Speagle, J. S., & Finkbeiner, D. 2019, *ApJ*, 887, 93
- Grevesse, N., & Sauval, A. J. 1998, *SSRv*, 85, 161
- Hall, O. J., Davies, G. R., Elsworth, Y. P., et al. 2019, *MNRAS*, 486, 3569
- Hekker, S. 2020, *Frontiers in Astronomy and Space Sciences*, 7, 3
- Heney, L., Vardya, M. S., & Bodenheimer, P. 1965, *ApJ*, 142, 841
- Herwig, F. 2000, *A&A*, 360, 952
- Ho, A. Y. Q., Rix, H.-W., Ness, M. K., et al. 2017, *ApJ*, 841, 40
- Howe, R., Chaplin, W. J., Basu, S., et al. 2020, *MNRAS*, 493, L49
- Huber, D., Stello, D., Bedding, T. R., et al. 2009, *Communications in Asteroseismology*, 160, 74
- Huber, D., Zinn, J., Bojsen-Hansen, M., et al. 2017, *ApJ*, 844, 102
- Hunter, J. D. 2007, *Computing in Science & Engineering*, 9, 90
- Jackson, R. J., & Jeffries, R. D. 2014, *MNRAS*, 441, 2111
- Jermyn, A. S., Bauer, E. B., Schwab, J., et al. 2023, *ApJS*, 265, 15
- Jiang, C., Wu, T., Feinstein, A. D., et al. 2023, *ApJ*, 945, 20
- Jiménez, A., García, R. A., Pérez Hernández, F., & Mathur, S. 2015, *A&A*, 583, A74
- Jimenez, R., Flynn, C., MacDonald, J., & Gibson, B. K. 2003, *Science*, 299, 1552
- Joyce, M., & Chaboyer, B. 2018a, *ApJ*, 864, 99
- . 2018b, *ApJ*, 856, 10
- Joyce, M., Johnson, C. I., Marchetti, T., et al. 2023, *ApJ*, 946, 28
- Joyce, M., & Tayar, J. 2023, *Galaxies*, 11, 75
- Kallinger, T. 2019, arXiv e-prints, arXiv:1906.09428
- Kallinger, T., Beck, P. G., Stello, D., & Garcia, R. A. 2018, *A&A*, 616, A104
- Kallinger, T., Hekker, S., Mosser, B., et al. 2012, *A&A*, 541, A51
- Karlslose, K. G. 2019, Master's thesis, Aarhus University
- Khan, S., Hall, O. J., Miglio, A., et al. 2018, *ApJ*, 859, 156
- Khan, S., Miglio, A., Mosser, B., et al. 2019, *A&A*, 628, A35
- Kjeldsen, H., & Bedding, T. R. 1995, *A&A*, 293, 87
- Lebreton, Y., & Goupil, M. J. 2014, *A&A*, 569, A21

- Lebreton, Y., Goupil, M. J., & Montalbán, J. 2014, in *EAS Publications Series*, Vol. 65, *EAS Publications Series*, ed. Y. Lebreton, D. Valls-Gabaud, & C. Charbonnel, 99–176
- Li, T., Bedding, T. R., Christensen-Dalsgaard, J., et al. 2020, *MNRAS*, 495, 3431
- Li, T., Bedding, T. R., Huber, D., et al. 2018, *MNRAS*, 475, 981
- Li, T., Li, Y., Bi, S., et al. 2022, *ApJ*, 927, 167
- Li, Y., Bedding, T. R., Stello, D., et al. 2021, *MNRAS*, 501, 3162
- . 2023, *MNRAS*, 523, 916
- Lightkurve Collaboration, Cardoso, J. V. d. M., Hedges, C., et al. 2018, *Lightkurve: Kepler and TESS time series analysis in Python*, *Astrophysics Source Code Library*
- Lindsay, C. J., Ong, J. M. J., & Basu, S. 2024, *ApJ*, 965, 171
- Magic, Z., Collet, R., Asplund, M., et al. 2013, *A&A*, 557, A26
- Magic, Z., Weiss, A., & Asplund, M. 2015, *A&A*, 573, A89
- McKeever, J. M., Basu, S., & Corsaro, E. 2019, *ApJ*, 874, 180
- Metcalfe, T. S., Creevey, O. L., Doğan, G., et al. 2014, *ApJS*, 214, 27
- Miglio, A., Chiappini, C., Mackereth, J. T., et al. 2021, *A&A*, 645, A85
- Mombarg, J. S. G., Van Reeth, T., & Aerts, C. 2021, *A&A*, 650, A58
- Montalbán, J., Miglio, A., Noels, A., Scuflaire, R., & Ventura, P. 2010, *ApJL*, 721, L182
- Montalbán, J., Mackereth, J. T., Miglio, A., et al. 2021, *Nature Astronomy*, 5, 640
- Mosser, B., Belkacem, K., Goupil, M. J., et al. 2011, *A&A*, 525, L9
- Nguyen, C. T., Costa, G., Girardi, L., et al. 2022, *A&A*, 665, A126
- Noll, A., Basu, S., & Hekker, S. 2024, *A&A*, 683, A189
- Ong, J. M. J., & Basu, S. 2020, *ApJ*, 898, 127
- Ong, J. M. J., Basu, S., Lund, M. N., et al. 2021a, *ApJ*, 922, 18
- Ong, J. M. J., Basu, S., & Roxburgh, I. W. 2021b, *ApJ*, 920, 8
- Ong, J. M. J., Lund, M. N., Basu, S., et al. 2022, in *Cambridge Workshop on Cool Stars, Stellar Systems, and the Sun*, *Cambridge Workshop on Cool Stars, Stellar Systems, and the Sun*, 1
- OpenAI. 2023, *arXiv e-prints*, *arXiv:2303.08774*
- Paxton, B., Bildsten, L., Dotter, A., et al. 2011, *ApJS*, 192, 3
- Paxton, B., Cantiello, M., Arras, P., et al. 2013, *ApJS*, 208, 4
- Paxton, B., Marchant, P., Schwab, J., et al. 2015, *ApJS*, 220, 15
- Paxton, B., Schwab, J., Bauer, E. B., et al. 2018, *ApJS*, 234, 34
- Paxton, B., Smolec, R., Schwab, J., et al. 2019, *ApJS*, 243, 10
- Peimbert, M., & Torres-Peimbert, S. 1974, *ApJ*, 193, 327
- Pinsonneault, M. H., Elsworth, Y. P., Tayar, J., et al. 2018, *ApJS*, 239, 32
- Planck Collaboration, Ade, P. A. R., Aghanim, N., et al. 2016, *A&A*, 594, A13
- Reyes, C., Stello, D., Hon, M., et al. 2024, *arXiv e-prints*, *arXiv:2407.03526*
- Sahlholdt, C. L., & Silva Aguirre, V. 2018, *MNRAS*, 481, L125
- Salaris, M., Cassisi, S., Schiavon, R. P., & Pietrinferni, A. 2018, *A&A*, 612, A68
- Samadi, R., Belkacem, K., Dupret, M. A., et al. 2012, *A&A*, 543, A120
- Schönhut-Stasik, J., Zinn, J. C., Stassun, K. G., et al. 2023, *arXiv e-prints*, *arXiv:2304.10654*
- Serenelli, A. M., Bergemann, M., Ruchti, G., & Casagrande, L. 2013, *MNRAS*, 429, 3645
- Sharma, S., Stello, D., Bland-Hawthorn, J., Huber, D., & Bedding, T. R. 2016, *ApJ*, 822, 15
- Silva Aguirre, V., Casagrande, L., Basu, S., et al. 2012, *ApJ*, 757, 99
- Silva Aguirre, V., Davies, G. R., Basu, S., et al. 2015, *MNRAS*, 452, 2127
- Silva Aguirre, V., Lund, M. N., Antia, H. M., et al. 2017, *ApJ*, 835, 173
- Silva Aguirre, V., Stello, D., Stokholm, A., et al. 2020, *ApJL*, 889, L34
- Smith, J. C., Stumpe, M. C., Van Cleve, J. E., et al. 2012, *PASP*, 124, 1000
- Somers, G., & Pinsonneault, M. H. 2015, *ApJ*, 807, 174
- Sreenivas, K. R., Bedding, T. R., Li, Y., et al. 2024, *arXiv e-prints*, *arXiv:2401.17557*
- Stumpe, M. C., Smith, J. C., Van Cleve, J. E., et al. 2012, *PASP*, 124, 985
- Tassoul, M. 1980, *ApJS*, 43, 469
- Tayar, J., Claytor, Z. R., Huber, D., & van Saders, J. 2022, *ApJ*, 927, 31
- Tayar, J., Somers, G., Pinsonneault, M. H., et al. 2017, *ApJ*, 840, 17
- Tian, Z., Bi, S., Bedding, T. R., & Yang, W. 2015, *A&A*, 580, A44
- Torres, G., & Ribas, I. 2002, *ApJ*, 567, 1140
- Townsend, R. 2020, *MESA SDK for Linux*

- Townsend, R. H. D., & Teitler, S. A. 2013, *MNRAS*, 435, 3406
- Trampedach, R., Stein, R. F., Christensen-Dalsgaard, J., Nordlund, Å., & Asplund, M. 2014, *MNRAS*, 445, 4366
- Valle, G., Dell’Omodarme, M., Prada Moroni, P. G., & Degl’Innocenti, S. 2019, *A&A*, 623, A59
- Valle, G., Dell’Omodarme, M., Tognelli, E., Prada Moroni, P. G., & Degl’Innocenti, S. 2018, *A&A*, 619, A158
- van der Walt, S., Colbert, S. C., & Varoquaux, G. 2011, *Computing in Science and Engineering*, 13, 22
- Verma, K., Raodeo, K., Basu, S., et al. 2019, *MNRAS*, 483, 4678
- Viani, L. S., Basu, S., Chaplin, W. J., Davies, G. R., & Elsworth, Y. 2017, *ApJ*, 843, 11
- Viani, L. S., Basu, S., Ong J., M. J., Bonaca, A., & Chaplin, W. J. 2018, *ApJ*, 858, 28
- Virtanen, P., Gommers, R., Oliphant, T. E., et al. 2020, *Nature Methods*, 17, 261
- Vrard, M., Mosser, B., & Samadi, R. 2016, *A&A*, 588, A87
- Wang, C., Huang, Y., Zhou, Y., & Zhang, H. 2023a, *A&A*, 675, A26
- Wang, Y., Li, T., Bi, S., Bedding, T. R., & Li, Y. 2023b, *ApJ*, 953, 182
- Wes McKinney. 2010, in *Proceedings of the 9th Python in Science Conference*, ed. Stéfan van der Walt & Jarrod Millman, 56 – 61
- Wu, Y., Xiang, M., Bi, S., et al. 2018, *MNRAS*, 475, 3633
- Xiang, M., & Rix, H.-W. 2022, *Nature*, 603, 599
- Yıldız, M., Çelik Orhan, Z., & Kayhan, C. 2016, *MNRAS*, 462, 1577
- Ying, J. M., Chaboyer, B., Boudreaux, E. M., et al. 2023, *AJ*, 166, 18
- Yu, J., Bedding, T. R., Stello, D., et al. 2020, *MNRAS*, 493, 1388
- Yu, J., Huber, D., Bedding, T. R., et al. 2018, *ApJS*, 236, 42
- Zhou, Y., Asplund, M., Collet, R., & Joyce, M. 2020, *MNRAS*, 495, 4904
- Zhou, Y., Christensen-Dalsgaard, J., Asplund, M., et al. 2023, *arXiv e-prints*, arXiv:2310.20050
- Zinn, J. C., Pinsonneault, M. H., Bildsten, L., & Stello, D. 2023, *MNRAS*, 525, 5540
- Zinn, J. C., Pinsonneault, M. H., Huber, D., et al. 2019, *ApJ*, 885, 166